Australian Black Summer smoke observed by lidar at the French Antarctic station Dumont d'Urville

Florent Tencé, Julien Jumelet, Slimane Bekki, Sergey Khaykin, Alain Sarkissian, Philippe Keckhut

JGR Atmospheres

RESEARCH ARTICLE
10.1029/2021JD035349

Special Section:
Stratospheric aerosol during the post Pinatubo era: processes, interactions, and impact

Australian Black Summer Smoke Observed by Lidar at the French Antarctic Station Dumont d'Urville

Florent Tencé[1], Julien Jumelet[1], Slimane Bekki[1], Sergey Khaykin[1], Alain Sarkissian[1], and Philippe Keckhut[1]

[1]LATMOS, Laboratoire Atmosphères, Milieux, Observations Spatiales, UMR CNRS, IPSL, Sorbonne University/UVSQ, Paris, France

Abstract In the follow-up of the Australian "Black Summer" event that persisted from August 2019 to March 2020, we present the optical properties of the stratospheric aerosols injected into the atmosphere by these wildfires. The outbreak of pyrocumulonimbus (PyroCb) activity triggered between 2019/12/29 and 2020/01/04 has raised the stratospheric aerosol load of the Southern Hemisphere to unprecedented levels. Long-range transport brought some of the plumes down to the Antarctic region, where general circulation patterns kept them circling around the continent. The 532 nm Rayleigh/Mie/Raman ground-based lidar of the French Antarctic station Dumont d'Urville (66.6°S–140°E) acquired unprecedented time series of these carbonaceous aerosols starting approximately 20 days after the injection and up to the most recent measurements in October 2019 where local radiosonde reported anomalous ozone depletion as compared to the decadal average. The lidar provides a first and unique time series at high vertical and temporal resolution, complemented by satellite measurements from Ozone Monitoring Instrument, Ozone Mapping and Profiler Suite, and Microwave Limb Sounder. Aerosol backscatter ratio decreases from 1.9 to 1.2 between January and June 2020. Aerosol origin and persistence are characterized, as well as their optical properties and vertical distribution over several months.

Plain Language Summary Major wildfires are now known to significantly contribute to the stratospheric aerosol load, which in turn may have consequences at the global scale. The deep convection and radiative uplift processes that they can spark, now colloquially referred to as pyroconvection, can inject significant quantities of aerosols into the stratosphere. The major wildfires that raged in Australia at the end of 2019 are a case in point: they injected an unprecedented amount of material into the stratosphere. After some weeks and due to the general circulation patterns, a part of this material ended up trapped above the Antarctic region. The lidar located at the French Antarctic station Dumont d'Urville had a unique opportunity to probe these stratospheric aerosols for an extended time period, allowing to observe the evolution in time of their optical properties over months. This study presents these valuable measurements which contribute to our knowledge of biomass-originated stratospheric aerosols and highlights the importance of operational ground-based instrumental capabilities and coverage at high latitudes.

Key Points:

- 2019–2020 Australian bushfires injected an unprecedented amount of aerosol into the stratosphere with impact at polar latitudes
- Longest ground-based lidar smoke aerosol record acquired at Dumont d'Urville with persistent 532 nm scattering ratio throughout the year 2020
- Simultaneous presence of polar stratospheric clouds and smoke aerosols were observed during the wintertime

Supporting Information:

Supporting Information may be found in the online version of this article.

Correspondence to:

F. Tencé,
florent.tence@latmos.ipsl.fr

Citation:

Tencé, F., Jumelet, J., Bekki, S., Khaykin, S., Sarkissian, A., & Keckhut, P. (2022). Australian Black Summer smoke observed by lidar at the French Antarctic station Dumont d'Urville. *Journal of Geophysical Research: Atmospheres*, *127*, e2021JD035349. https://doi.org/10.1029/2021JD035349

Received 4 JUN 2021
Accepted 7 JAN 2022

1. Introduction

Australia experienced an unprecedented fire season from August 2019 to March 2020, now colloquially named "Black Summer" (Davey & Sarre, 2020). While the country regularly experiences seasonal bushfires (Cheney, 1976; Lucas et al., 2007; Sharples et al., 2016), the 2019/2020 events broke records in both duration and intensity (Davey & Sarre, 2020). High temperatures and severe droughts are key parameters influencing the extent of bushfires (McArthur, 1967). A warming climate, therefore, favors a higher frequency of severe wildfire episodes during the fire season (Clarke et al., 2013; Dowdy et al., 2019; Hennessy, 2006). For this reason, it is critical to study their impact on a large scale as transport processes that may, for example, involve the development of local PyroCumulonimbus (PyroCb) can inject large quantities of material directly into the stratosphere, where the residence time of aerosols is not limited by cloud scavenging and precipitation.

The dynamics of the stratospheric Antarctic winters at high latitudes are characterized by strong rotating winds encircling the Antarctic continent from around May to October. This stratospheric cyclonic wind pattern, referred to as the Antarctic polar vortex, maintains the cold Antarctic central region relatively isolated from mid-latitude warmer air mass incursions during the winter. Winter polar temperatures are generally so low that different types

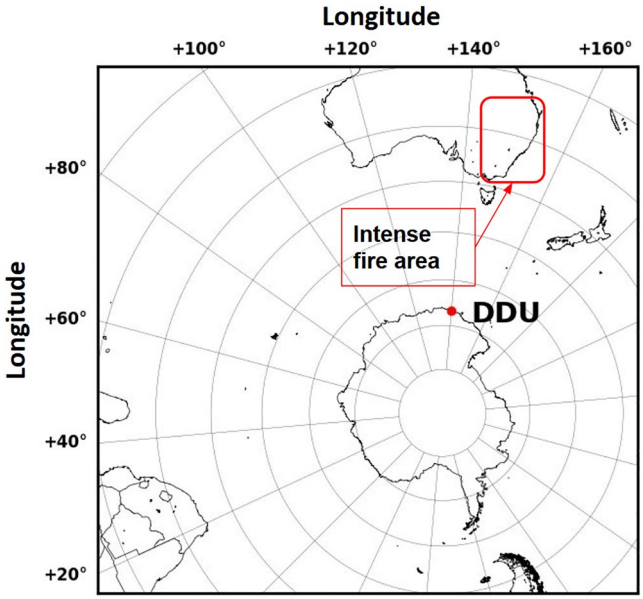

Figure 1. Map of Australia and the French Antarctic Station Dumont d'Urville (66°S–140°E). The red frame encloses the intense fire area (Peterson et al., 2021).

of Polar Stratospheric Clouds (PSC) form within the polar vortex. PSCs are essential in the formation of the ozone hole because, through their heterogeneous chemistry, they convert stratospheric reservoir species ($ClONO_2$, HCl, HBr) into active radicals (ClO, BrO) that catalyze ozone destruction.

Stratospheric aerosols have an important direct impact on the Earth's radiative budget by reflection and absorption of solar radiation, along with other indirect effects like enhancing nucleation processes (Charlson et al., 1992; Penner et al., 2001). While the role of stratospheric aerosols has now been studied for years, a lot remains to be understood as recent investigations also lead to additional challenges (for instance regarding stratospheric trends, the effect of climate change [Kremser et al., 2016], or the contribution of wildfires to the stratospheric aerosol load [Khaykin et al., 2020; Peterson et al., 2017, 2021]). Moderate volcanic activity is now acknowledged as a major source of stratospheric sulphate aerosols (Bègue et al., 2017; Khaykin et al., 2018), especially in the case of regular eruptions. The separation of quiescent and volcanic regimes is still a challenge for the monitoring networks despite recent improvements, especially in the spaceborne capabilities. Volcanic aerosols impact the climate, as well as enhance stratospheric ozone depletion (Kremser et al., 2016). Obviously, the most pronounced impacts occur during major eruptions. For example, the Mount Pinatubo eruption led to a global surface cooling of around 0.5°C. Furthermore, many uncertainties still remain on the scale and strength of the impact of biomass-originated aerosols injected into the stratosphere. A recent study (Martinsson et al., 2019) suggests that the amount of carbonaceous aerosols in the stratosphere is still underestimated. In addition, in situ measurement campaigns remain rare and detection of fine aerosol plumes is difficult. From the ground, the fine plumes may be missed due to the static position of the instrument and moving air masses. From a spaceborne geometry, instrumental calibration gets of primary importance due to the fine associated optical properties. As for the lidar instrument, aerosol speciation requires an extensive set of observables (scattering ratio or color ratios, depolarization ratio, lidar ratio when available) along with a good Signal-to-Noise Ratio (SNR).

Strong fire activity triggering pyroCb events are now thoroughly documented (Dowdy et al., 2017, 2019; Fromm et al., 2006, 2010; McRae et al., 2015; Peterson et al., 2017; Tory et al., 2018). Several important pyroCb events occurred between 29 December 2019 and 4 January 2020 (Kablick et al., 2020; Khaykin et al., 2020) injecting a considerable amount of fire smoke containing aerosols into the stratosphere. This material then experienced long range transport over thousands of kilometers (Khaykin et al., 2020; Ohneiser et al., 2020) to finally, for a fraction of it, reach high southern latitudes over the Antarctic region. Although stratospheric transport of biomass burning aerosol over the Antarctic region has already been confirmed (Fiebig et al., 2009; Jumelet et al., 2020), the 2019/2020 events reached an unprecedented level in terms of ground emissions and atmospheric impact (Davey & Sarre, 2020; Kablick et al., 2020; Khaykin et al., 2020). Using top of the atmosphere flux measurements, Hirsch and Koren (2021) estimated that the injected aerosols led to cooling by more than 1.0 ± 0.6 watts per square meter over cloud-free oceanic waters.

A large number of satellite missions monitor the global evolution of such stratospheric events both in terms of gas composition (Microwave Limb Sounder - MLS, Ozone Monitoring Instrument - OMI, Infrared Atmospheric Sounding Interferometer - IASI, Atmospheric Infrared Sounder - AIRS) and particle content (Ozone Mapping and Profiler Suite - OMPS, Cloud-Aerosol Lidar and Infrared Pathfinder Satellite Observation - CALIOP aboard CALIPSO). However, fine plumes of aged aerosols, either containing sulfur or carbon, tend to display overlapping optical properties that are often close to the detection threshold of spaceborne active sounders (Baars et al., 2019; Hu et al., 2019; Jumelet et al., 2020). Ground-based lidar facilities remain best suited to complement satellite instruments due to their fine vertical resolution and sampling rate, at the cost of coverage especially in polar areas due to the low density of monitoring stations.

In this study, we use lidar measurements from the French Antarctic station Dumont d'Urville (see Figure 1 for the locations of DDU and Australian 2019–2020 wildfire area), along with satellite measurements and trajectory

modeling to characterize the smoke aerosols originated from the Australian 2019/2020 wildfires. First, in Section 2, we provide a brief description of the 2019/2020 Australian bushfire event. Second, the instruments and data specifications are presented in Section 3. Then, in Section 4, our observations and results are discussed and characterization of the wildfire aerosols is provided along with estimates of the optical properties that we compare against the results provided in the literature available on similar events. Conclusions are provided in Section 5.

2. Event Description

The fire season started in August 2019 (Davey & Sarre, 2020) in the regions of Queensland and New South Wales. The major fires were declared to be under control and extinguished by early March. The events referred to as "Black Summer" spread over several states and burnt a total area of ∼103,000 km^2, almost twice as much as any previous bushfire event in Australia (Davey & Sarre, 2020). The fires burnt to ashes more than 8 million ha of native forest, mostly eucalyptus forest (Peterson et al., 2021), and significantly affected local biodiversity along with many casualties. The smoke generated by these fires drastically reduced air quality in the cities of Queensland, New South Wales, Australian Capital Territory, and Victoria regions, leading to an unprecedented smoke-related health burden (Borchers Arriagada et al., 2020).

The factors leading to such an important fire season are numerous, mainly severe droughts and extremely hot temperatures (Adams et al., 2020; Nolan et al., 2020). Several studies investigate the specific combination of climatic drivers (the El Nino Southern Oscillation, the Indian Ocean Dipole, and the South Annular Mode) that could lead to such climatic conditions in Australia (Cai et al., 2009; Lim et al., 2019). Lim et al. (2019) suggested a link between the Australian climatic conditions in 2019–2020 and the important Sudden Stratospheric Warming that occurred in the Southern Hemisphere in 2019 (Safieddine et al., 2020).

At the end of December 2019, several pyroCb events injected significant smoke plumes into the stratosphere, enabling large scale travel: Kablick et al. (2020) accounted for at least 18 pyroCb events between 2019/12/29 and 2020/01/04. On 2020/01/05, the smoke plume had reached Chile, traveling more than 11,000 km (Ohneiser et al., 2020). Wildfire aerosols progressively spread across the southern hemispheric stratosphere, significantly increasing its aerosol concentration. The present study only focuses on the specific smoke plumes that reached high southern latitudes and circulated around Antarctica. Approximately 20 days after the pyroCb events, the smoke from Australian Black Summer was detected for the first time at the French Antarctic station Dumont d'Urville.

3. Instruments and Data Sources

3.1. Dumont d'Urville Lidar

Since April 1989, an aerosol/cloud lidar system is in operation at the French Antarctic station DDU (66°S–140°E) in the framework of the Network for Detection of Atmospheric Composition Changes (NDACC). Originally designed as a PSC monitoring instrument, its capabilities have been extended to study aerosol and cirrus clouds in the Antarctic atmosphere. The measurement calendar focuses on the PSC season with nighttime setup, still, the exceptional events we report lead us to carry out summer time measurements.

The Rayleigh/Mie/Raman lidar operates at the 532 nm wavelength. N_2 vibrational Raman scattering at 607 nm is also acquired. A complete description of both the instrumental design and inversion procedure is featured in David et al. (2012). The Nd:YAG laser source emits at 10 Hz frequency with around 250 mJ emitted power in the visible. Backscattered photons are collected on a collocated 80 cm diameter Newton telescope. A polarizing cube at the reception splits the beam into two components polarized parallel and perpendicular to the laser emission for the 532 nm wavelength, each component is recorded and inverted to gain access to the depolarization ratio. In this study, we use the aerosol depolarization value defined as the ratio between the perpendicular and parallel particulate backscatter coefficients.

Aerosol vertical profiles will be considered as Backscattering Ratio or Scattering Ratio profiles (hereafter called SR) expressed as the ratio of the total scattering (i.e., including Mie Scattering) to the molecular scattering at a given altitude. Potential saturation effects in the tropopause, as well as background noise at mesospheric altitudes, are removed from lidar signals. The best time integration window is selected based on the homogeneity of the scene featured on the attenuated SR. Finally, signal inversion is performed using the Klett-Fernald formalism

(Fernald, 1984; Klett, 1981, 1985) to derive individual SR profiles. The lidar inversion is sensitive to the molecular density and the clear-air reference altitude. Collocated radiosondes are used to estimate reference atmospheric density and interpolation. Scaling to ERA5 daily meteorological data is done at balloon burst altitude (between 20 and 30 km, depending on the season) and clear-air altitude is set between 28 and 32 km according to the signal dynamics. Required Lidar ratio (LR) estimates are based on background aerosols (LR = 50 sr) climatological values and for the current study, when the SNR is high enough we also use the Raman derived LR from the 607 nm channel using the formalism expressed in Ansmann et al. (1992) and Ohneiser et al. (2020). Still, the laser emitted power is only sufficient to derive particle extinction from the 607 nm N2 Raman channel up to the 20 km altitude most of the time, which is high enough for investigating this event.

The SR uncertainty is first related to statistical fluctuations of the measured lidar signal with random detection processes estimated using a Poisson distribution from the number of photons received. It is around 2% on the parallel channel and below 5% on the perpendicular channel for smoke layers, as increased backscatter leads to smaller uncertainty. In this paper, the uncertainty on the Rayleigh contribution is estimated to be below 2% using sensitivity calculations of the Rayleigh backscatter coefficient accounting for temperature differences derived from comparisons between ERA5 and local radiosondes. For the lidar ratio, using the 607 nm N_2 Raman channel helps in decreasing the uncertainty originating from the LR assumption in the Klett procedure, which is expected to be around 20% (David-Beausire et al., 1998). Based on years of aerosol lidar data, the total uncertainty on the SR is estimated to be around 7% on $SR_{//}$ up to 28 km, following the approach of David-Beausire et al. (1998) and Chazette et al. (1995). On the perpendicular channel, the signal has a lower SNR, leading to a greater uncertainty on the clear-air reference taken above 25 km during the inversion. The retrieval procedure is described in detail in David-Beausire et al. (1998) giving an overall altitude-dependent uncertainty from 10% to 30%. Depolarizing material such as smoke aerosols generates higher perpendicular backscatter coefficients, resulting in higher SNRs and therefore lower uncertainties. The discussion part only uses estimates of the optical properties up to the 20 km altitude and using a batch of clear-air night-time aerosol lidar data acquired at Dumont d'Urville during April (before the PSC season) in the last couple of years, we statistically estimate the uncertainty on $SR_{\perp}$ around 20%.

Overall, The total 532 nm SR is calculated from the parallel and perpendicular backscatter ratio accounting for the influence of the molecular depolarization ratio (0.44% in this case – Behrendt & Nakamura, 2002). Obviously, the longer the lidar time integration window, the lower the uncertainty. Using the averaged SR values presented in this paper as a reference and considering the above uncertainties on both $SR_{//}$ and $SR_{\perp}$, the total uncertainty on the scattering ratio is therefore estimated at around 30% for profiles determined on integration windows of less than 1h30, and 20% beyond 2h time integration. As for the depolarization ratio, following the methodology also presented in David et al. (2012) and still assuming larger uncertainties on the aerosol depolarization ratio δ(z) rather than on the linear volume depolarization ratio at relevant altitudes in this paper we estimate the error on δ(z) at around 30%.

3.2. Ozone Mapping and Profiler Suite (OMPS) Satellite - Limb Profiler

The Limb Profiler (LP) instrument is part of the Ozone Mapping and Profiler Suite onboard the Suomi National Polar-orbiting Partnership (NPP) satellite launched in October 2011. The OMPS/LP performs simultaneous measurements of the Earth's sun-lit limb. The instrument provides radiance profiles for wavelengths ranging from 290 to 1,000 nm. The OMPS/LP has global spatial coverage and about 14.5 orbits per day each measuring three limb profiles thanks to three slits: a central one along the orbital track and two slits that are offset by 4.25° from the orbital track. The vertical resolution of the retrieved profiles is approximately 1.8 km. More detailed information on the OMPS/LP instrument can be found in (Flynn et al., 2014; Jaross et al., 2014; Rault & Loughman, 2013). In this study, we used the aerosol extinction product, which is based on the radiance measurements at 675 nm. The version 1.5 aerosol algorithm described in (Chen et al., 2018) is used to retrieve aerosol extinction vertical profiles in km^{-1}.

3.3. Ozone Measuring Instrument (OMI) Satellite

Launched in July 2004, the Dutch-Finnish Ozone Monitoring Instrument (OMI) is one of the four sensors onboard the NASA Earth Observing System (EOS) Aura mission (Levelt et al., 2006). OMI is a spectrograph measuring the upwelling radiance at the top of the atmosphere in the 270–500 nm wavelength range (Torres

et al., 2007). Its spatial resolution ranges from 13 × 24 km at nadir to about 28 × 150 km at the extremes of the swath. OMI is dedicated to the monitoring of ozone, but criteria pollutants such as NO_2, SO_2, BrO, HCHO, OClO, and aerosols are also retrieved from OMI radiance measurements. It is therefore perfectly suited to detect smoke plumes and aerosols produced by volcanic eruptions or biomass fires.

The level 3 UV Aerosol Index (UV AI) product used in this study has a spatial resolution of 1° × 1°. This product is retrieved using the near-UV aerosol retrieval algorithm OMAERUV detailed in (Torres et al., 2007). The UV AI measures how the wavelength dependence of backscattered UV radiation from the probed atmosphere differs from that of a pure molecular atmosphere, that is, pure Rayleigh scattering. It is expressed as follows:

$$AI = 100 * \log\left(\frac{I_{360nm_{measured}}}{I_{360nm_{calculated}}}\right) \quad (1)$$

Therefore, the UV AI is positive when sounding absorbing aerosols, negative when sounding non-absorbing aerosols and close to zero for a theoretical unperturbed atmosphere. In this study, the UV AI data are smoothed on a 3 days window.

3.4. Microwave Limb Sounder (MLS) - Aura Satellite

The Microwave Limb Sounder (MLS) is one of the four instruments on board the NASA EOS Aura Mission, launched on 15 July 2004. MLS provides measurements of the atmospheric gaseous composition by detecting thermal microwave limb emission from a number of atmospheric molecules in the range from 118 GHz to 2.5 THz (Waters et al., 2006). Aura offers global coverage with 15 orbits per day on average. Unlike shorter-wavelength instruments, MLS offers the advantage to conduct measurements in the presence of ice clouds and aerosols.

In this study, the level 2 products of mixing ratio of carbon monoxide (CO) and water vapor (H_2O) are used to follow the stratospheric implications of the 2019–2020 Australian wildfires. Both products have a horizontal resolution of 165 × 3 km and a vertical resolution between 1.5 and 6 km. More information on these products can be found in (Livesey et al., 2007). According to the MLS data quality document, at the relevant pressure levels, the accuracy of MLS is 8%–15% for H_2O measurements and ±30% for CO measurements. In this study, both products are smoothed on a 10 days time window.

3.5. Hysplit Trajectories

The Hybrid Single Particle Lagrangian Integrated Trajectory (Hysplit) model developed by NOAA and Australia's Bureau of Meteorology was used to compute air parcel backward trajectories (Rolph et al., 2017; Stein et al., 2016). In this study, we use Hysplit in its standard setup to generate backward trajectories of air parcels in order to establish source-receptor relationships. The computed trajectories all end at DDU from January to June 2020 at altitudes between 10 and 20 km. The calculations were based on GDAS1 reanalysis data. The run duration is usually set between 200 and 315 hr in order to capture the long-range transport of aerosols detected at DDU.

4. Observation and Results

To get the most out of the ground-based lidar time series and link the measurements to the Australian fire event, the overall stratospheric aerosol load is first investigated using satellite data. Figure 2 displays the daily mean UV AI south of 30°S latitude (gray and black lines) and within a domain centered around DDU station (61.5–71.5°S, 130–150°E; red lines) for the year 2019/20 in comparison to the averaged value on the 10 previous years. This graph highlights the sheer impact of the Australian-originated plume injections as seen in the UV from OMI. The pyroCb events almost doubled the mean UV AI south of 30°S as compared to the 10 previous years. The red line, corresponding to the area around DDU, shows, as expected, a more progressive increase and also exceeds the decadal mean from January 1st.

The OMPS/LP instrument complements OMI measurements with spectral bands closer to the aerosol-sensitive spectral ranges. The 675 nm aerosol extinction product is well suited to aerosol plumes being close to the 532 nm lidar wavelength. The aerosol extinction is averaged in the area ranging from 61.6°S to 71.6°S and from 130°E

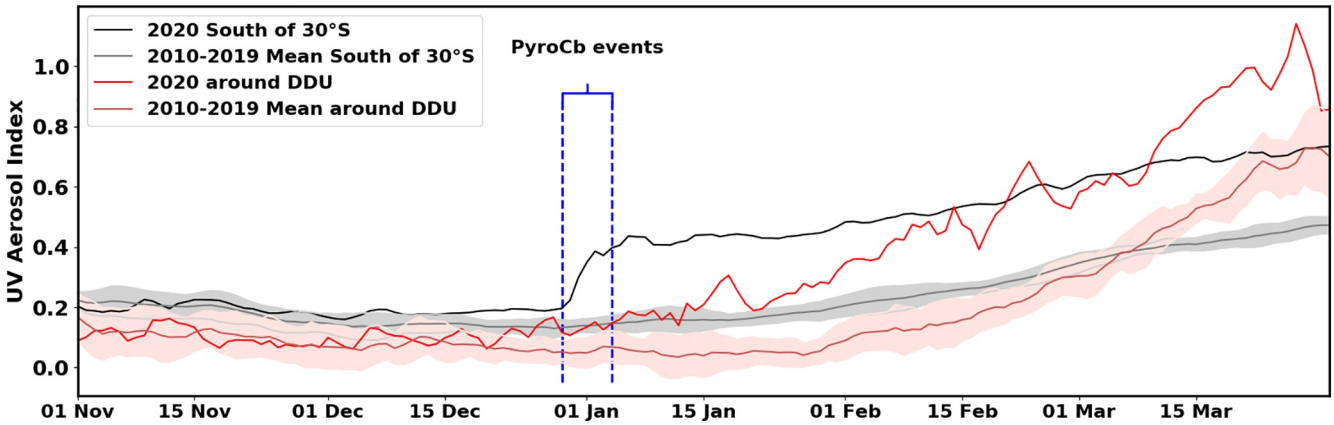

Figure 2. Mean Ozone Monitoring Instrument UV Aerosol Index south of 30°S (black line for 2019–2020, gray line for 2010–2019 mean) and in the domain 61.5°S-71.5°S; 130°E−150°E around Dumont dUrville station (red line for 2019–2020, pale red line for 2010–2019 mean). Standard deviation of the 10-year mean in shaded color. Dashed blue lines show the time period of the pyroCb injections reported by (Kablick et al., 2020).

to 150°E. Figure 3a is a time series of the aerosol extinction in this domain as a function of altitude, from 10.5 to 30.5 km.

In this time series, we note the sharp increase of the aerosol extinction starting on 2020/01/17 and 2020/01/18, with aerosol layers present within a broad layer between about 11 and 20 km. In order to compare the extracted OMPS data with DDU lidar measurements, we produced a time series of the lidar 532 nm scattering ratio shown in Figure 2b using the same time sampling. The white bands on this time series (Figure 3b) correspond to days where lidar measurements are not available. The instrument is designed for the winter season, and operability during the summer time is reduced, however during polar summer 2019/2020, the lidar is operated in daylight mode. The first aerosol signatures are detected between 2019/11/04 and 2019/11/08. Figure 3c shows a close-up of those early aerosol lidar measurements. During five consecutive days, the lidar at DDU detected a persistent signal slightly above 15 km, with a 532 nm SR around 1.2 and presented a depolarization ratio close to zero (not shown). Then the DDU lidar scene only features clear sky situations until 2020/01/12 when a low aerosol signal is detected.

The origin of the aerosol plume detected at DDU in early November remains unclear from the available datasets. It could be an early injection from the Australian wildfires but no significant stratospheric injections have been reported before 2019/12/29 (Khaykin et al., 2020; Kablick et al., 2020; Peterson et al., 2017). According to Kloss et al. (2021), it could also be sulfated aerosols injected by the Ulawun eruptions (2019/06/21 and 2019/08/03) since the authors showed that part of the volcanic material injected in the stratosphere was transported toward high southern latitudes (Kloss et al., 2021 - Figure 5). However, this hypothesis is not supported by the stratospheric CO increase measured by MLS (see right below - Figure 4) south of 65°S. Finally, fires that took place in South West Africa from June–August 2019 seem to be associated with high southern latitude aerosol transport, according to OMI UV AI maps (not shown) and OMPS UV AI publicly available on the EOSDIS Nasa Worldview platform. Considering the previous arguments, we favor the African wildfires origin. This example highlights that, despite extensive satellite coverage and instrumental spectral capabilities, it is not possible to conclude with certainty on the origin of an aerosol plume detected at DDU in November for five consecutive days.

Starting from 2020/01/19, strong aerosol signals with 532 nm SR above 1.4 were measured on an increasing altitude extent, which is consistent with OMPS-LP observations in Figure 3a. Behavior of the extinction follow the one of the SR assuming the aerosol population has a constant homogeneous chemical composition, hence, lidar ratio.

OMI UV Aerosol Index and OMPS 675 nm aerosol extinction presented in Figures 2 and 3 clearly show significantly distinct values from the background at the beginning of 2020 below 30°S and around DDU. The OMI and OMPS instruments measure the aerosol phase but to refine the event tracking it may be useful to also analyze the density of two gas phase chemical tracers typically linked to wildfires events and tracing pyroCb transport: CO and H_2O. We use MLS measurements as they cover high latitudes all year long. We compute the mean density of

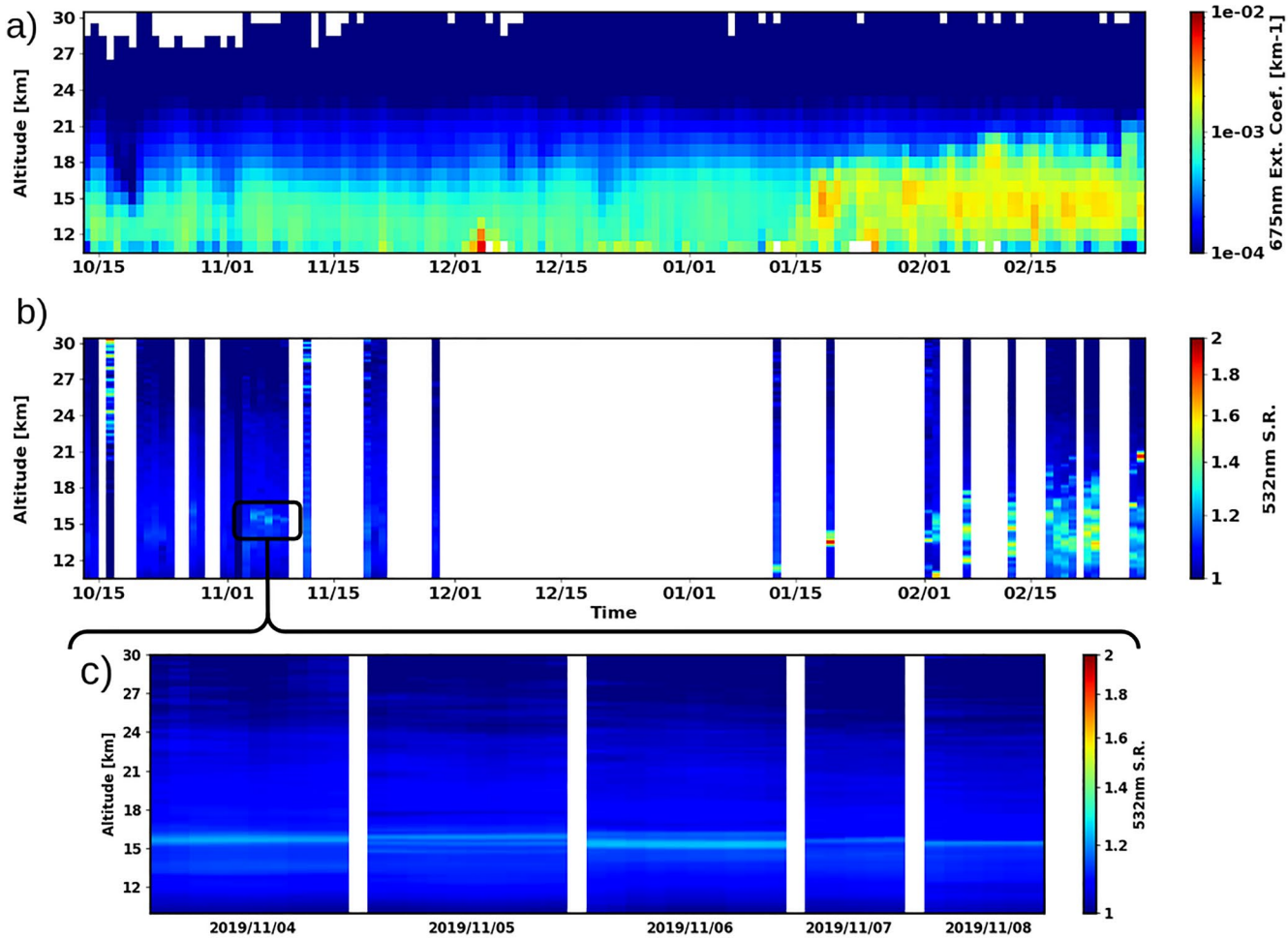

Figure 3. Time series from 2019/10/13 to 2020/02/29 of (a) Ozone Mapping and Profiler Suite 675 nm aerosol extinction coefficient (km^{-1}) averaged on the domain ranging from 61.6°S to 71.6°S and 130°E to 150°E and of (b) 532 nm scattering ratio (S.R.) measured by the lidar at the French Antarctic station Dumont dUrville. (c) Close-up of (b) time series from 2019/11/04 to 2019/11/08.

the species in two areas: above Antarctica (taken as below 65°S and over DDU [61.6°–71.6°S, 130°–150°E]) at two pressure levels, 146 hPa and 100 hPa. These levels correspond to the aerosol layers in the lower stratosphere: depending on the season, the 146 hPa level corresponds to altitudes between 12.5 and 13.5 km and the 100 hPa to altitudes between 14.7 and 16 km. Over these two areas, we compare in Figure 4 the CO and H_2O densities from July to June of the years 2019–2020 with the past decade's mean.

Both CO and H_2O densities reach above average values in 2019–2020. At 146 hPa over Antarctica (Figure 4c), we notice that CO and H_2O densities significantly increase as early as October 2019. This early increase is in agreement with the first aerosol measurements at DDU in November 2019 shown in Figure 3c. At 100 hPa over Antarctica (Figure 4a), the impact of the pyroCb events (delimited by the vertical black dashed lines) is clear. The 2019–2020 CO density, which is slightly above average since September 2019, sharply increases at the beginning of 2020. The behavior is smoother for the H2O mixing ratio at 100 hPa, but we still see that it clearly separates from the past 10 years standard deviation after the pyroCb events.

Above DDU, the variability of plume densities is higher due to the spatial sampling inside the smaller domain. Nevertheless, we notice the impact of the pyroCb events on the CO mixing ratio at both the 100 hPa and 146 hPa levels. This clear signature is visible from January 1st in Figures 4b and 4d. Due to the limited domain centered around the DDU station and the associated MLS uncertainties at the considered levels, stating the presence of smoke aerosol is only possible using additional analyses of smoke transport toward DDU.

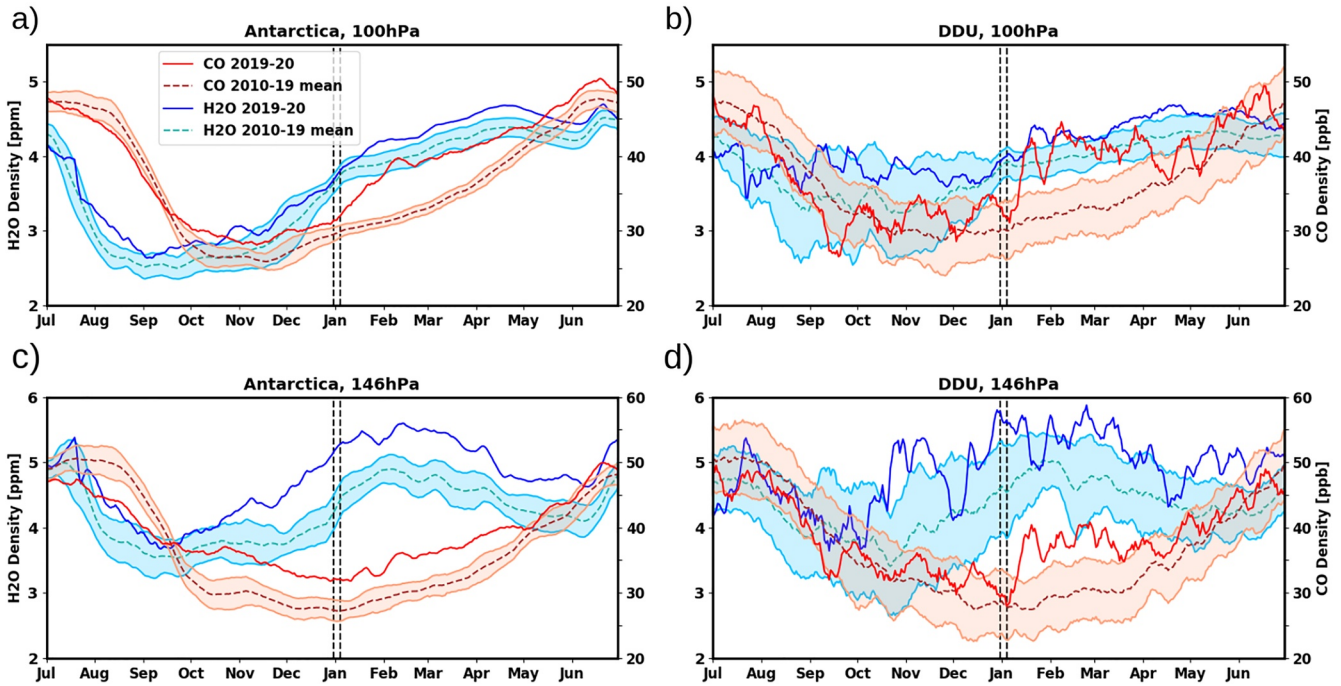

Figure 4. Microwave Limb Sounder concentration of H_2O (blue lines) and CO (red lines) at 100 hPa (top) and 146 hPa (bottom) above Antarctica (left) and above Dumont d'Urville (DDU) (right). The area around DDU includes latitudes between 61.6°S and 71.6°S and longitudes between 130°E and 150°E. Antarctica is taken as below the 65°S latitude line. The *x*-axis starts in July 2019 and ends in June 2020. The solid blue and red lines show the 2019–2020 concentrations while the dashed lines represent the mean for the 2010–2019 period. The shaded areas represent the standard deviations. The dashed black vertical lines delimit the period of the main pyroCb events of the 2019–2020 Black Summer.

The Hysplit backward trajectory presented in Figure 5 supports the above statement on the arrival of smoke aerosol above DDU since January. It shows that the air parcel at 13.5 km above DDU on 2020/01/19 at 16:00 UTC was 315hr earlier, that is, on 2020/01/06 at 13:00 UTC above South America. Figure 5a is a map of OMI UV AI averaged on 2020/01/06 and 2020/01/07. The part of the trajectory corresponding to 2020/01/06 and 2020/01/07 is highlighted in green. This zone indeed presents a high UV AI. Figure 5b shows the same Figure for 2020/01/13 and 2020/01/14. The zone around the trajectory highlighted in green shows a higher UV AI than average, directly coming from the smoke plumes produced by the bushfires in Australia.

On 2020/01/19 the lidar at DDU recorded a clear optical signature related to the Australian bushfire aerosols (Figure 6a). The time and altitude of the aerosol layer match the OMPS/LP data presented in Figure 3a and are also consistent with the OMI data of Figure 2. The aerosol layer was detected in the range between 12.9 and 14.6 km with a maximum 532 nm SR value of 1.9 at 13.5 km. At the beginning of the trajectory shown in Figure 5, the height is between 14 and 15.4 km which corresponds to the altitude of the aerosol layer on the 9 January described in Ohneiser et al., 2020. The authors mentioned an aerosol signature on January 5th in their introduction without information about its altitude so we cannot relate it to our observations.

From 2020/01/19 onwards the lidar measurements in DDU show numerous fine layers between 10 and 20 km. The time series of these measurements shown in Figure 6f is consistent with the horizontal transport of aerosol layers from the lower latitudes mentioned previously. Detection of smoke aerosols before the PSC season is possible because carbonaceous aerosols are expected to slightly depolarize, which is not the case for sulfated aerosols, being liquid droplets of H_2SO_4/H_2O. During the winter season and PSC presence, the optical signature of the Australian-originated aerosols blends with the stronger ones of PSC layers at 532 nm, both in SR and depolarization ratios. Nevertheless, clear air profiles throughout the winter season constantly display enhanced aerosol load optical properties that do not match the expected sulfated background values (i.e., above $SR > 1.1$).

Figure 6f shows that the SR values decrease with time before the beginning of the PSC season in late June. The lidar profiles shown in Figures 6a–6c are obtained with measurements on respectively 2020/01/19, 2020/02/01,

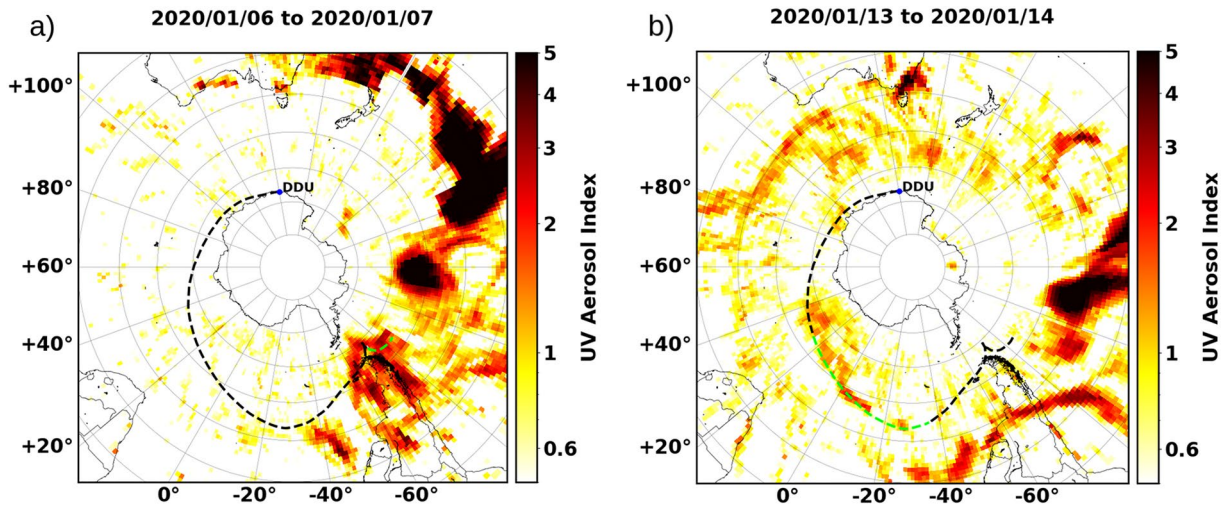

Figure 5. Maps of the Ozone Monitoring Instrument UV AI averaged between 2020/01/06 and 2020/01/07 (a) and between 2020/01/13 and 2020/01/14 (b). Hysplit backward trajectories of 315 hr ending at the French Antarctic station Dumont dUrville on 2020/01/19 at 16:00 UTC at 13.5 km is shown in black dashed lines. The parts of the trajectories corresponding to the relevant dates are highlighted in green.

and 2020/02/20 and illustrate this evolution more precisely. The distinct layers at various altitudes observed in the time series are most likely signatures of new and fine plumes coming from lower latitudes convoluted in the first weeks to plumes having experienced circular transport around the continent. This statement is supported by additional trajectories shown in Annex 1. Temperature profiles from local radiosondes shown in blue in Figures 6a

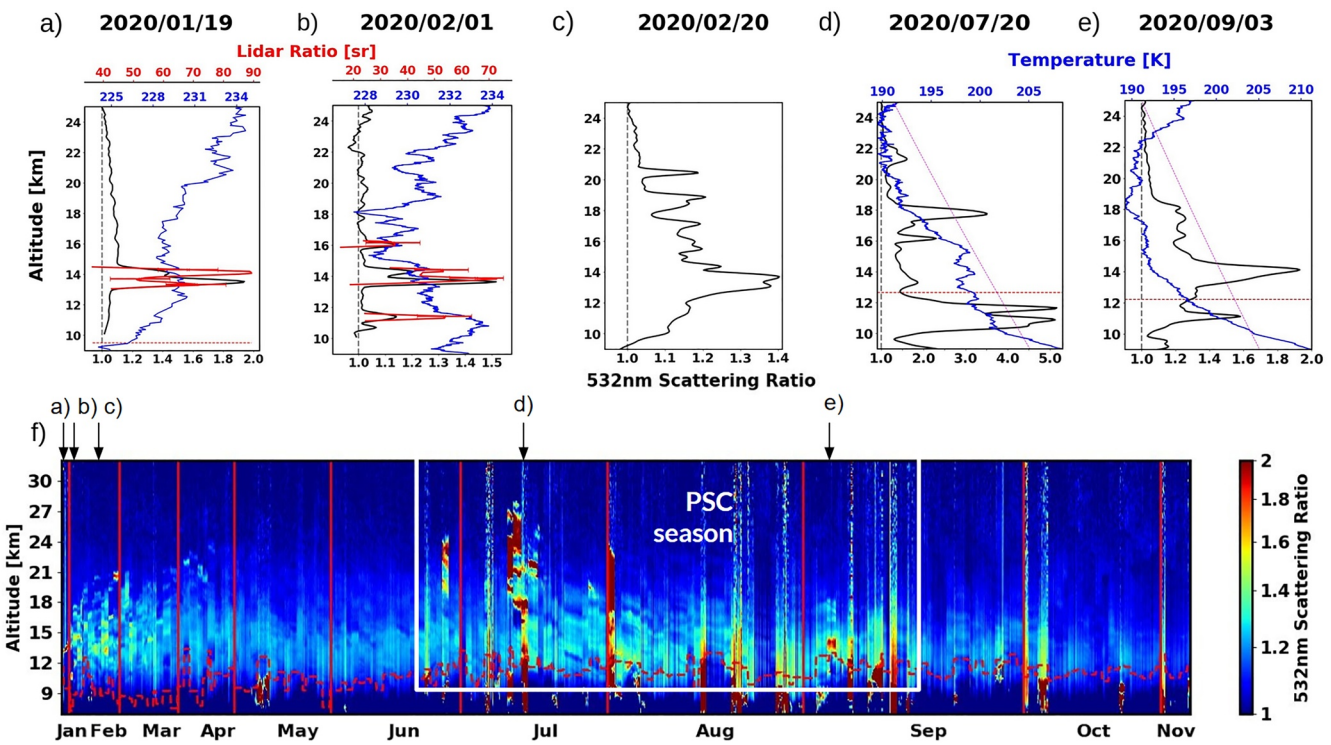

Figure 6. Lidar profiles acquired at Dumont dUrville on 2020/01/19 (a), 2020/02/01 (b), 2020/02/20 (c), 2020/07/20 (d), and 2020/09/03 (e) are shown. On (a) and (b) the Lidar Ratio is plotted in red. Temperature from local radiosondes are shown in blue when available, as well as T_{NAT} temperature threshold in purple dashed line on (d) and (e). Time series of the 532 nm scattering ratio from 2020/01/12 to 2020/11/16 at DDU (f). The dashed red line indicates the location of the dynamical tropopause. Time scale is not linear and depends on lidar operation possibilities.

and 6b exhibit local peaks at heights corresponding to the aerosol layers which indicate the absorption capacity of the carbonaceous aerosols.

Figures 6d and 6e show lidar profiles from measurements during the winter season, on the 2020/07/20 (Figures 6d) and 2020/09/03 (Figure 6e) with potential PSC presence. Temperature profiles from local radiosondes are shown in blue on Figures 6d and 6e and help discuss the nature of the detected scattering layers together with the Nitric Acid Trihydrate (NAT) formation temperature threshold (T_{NAT}) shown in purple dashed line. PSCs cannot form above this temperature threshold (Tritscher et al., 2021). On 2020/07/20 (Figure 6d), the layers around 13.5 and 16 km present SR values of 1.8 and 2.3 respectively. These layers correspond to temperatures slightly below T_{NAT} but correspond to local temperature peaks, which is not what is expected in presence of PSCs. Despite the SR values being higher than what is expected for aerosols, it is difficult to conclude the nature of these layers. The layer at 18 km is more straight-forward to analyze: the high SR of 3.5 and the temperature significantly below T_{NAT} clearly indicate a PSC presence. This analysis is also applicable to Figure 6e, where the temperature clearly below T_{NAT} tends to classify the layer around 14 km as PSC.

Estimates of the lidar ratio are plotted in red in Figures 6a and 6b with values peaking between 70 and 90 sr within the plumes. The time average of the profiles is chosen high enough to keep the SNR high but no more than 2 hr to not blend the plume signal to clear air when the filament is not within the lidar field of view anymore. Those LR values are comparable to what Ohneiser et al. (2020) retrieved in Chile, weeks in advance at lower latitudes. Impact of some weeks of transport does not seem to alter the LR, but pushing the analysis is not really possible because retrievals with different time integration and pre-processing of the signal lead to an overall 15–20 sr uncertainty which is relatively high considering sulphate aerosols are expected to have LRs between 50 and 60 sr.

Still, the successful retrieval of the optical properties of these aerosols allows us to take advantage of the high vertical resolution (as compared to passive sensors) to gain access to the fine-scale plume evolution. Figure 7 shows four examples of lidar curtains obtained in 2020. Figures 7a and 7b present summertime observations, respectively on 2020/02/06 and 2020/03/23, while Figures 7c and 7d present observations during the PSC season, respectively on 2020/07/26 and 2020/08/05, together with the corresponding temperature profiles from local radiosondes (blue lines) and ERA5 reanalysis (green line). Associated depolarization ratio profiles are also shown (red lines). The laminated structure of the aerosol layers is clearly visible, especially in the earlier months of the year (Figure 7a) with higher backscatter values, but remain present over the months. Two elements come out of the comparison between Figures 7a and 7b. First, the 532 nm SR values decrease with time: they peak at 1.54 on 2020/02/06 and drop to 1.31 on 2020/03/23. This consistent trend is observed from the first aerosol measurements in 2020 until mid-June and the beginning of winter. Second, a larger amount of layers can be seen with an increased vertical extent in the early weeks. As a result of the high absorption property of carbonaceous aerosols, temperature profiles of Figures 7a and 7b exhibit a local positive anomaly at heights corresponding to the aerosol layers which are also partly resolved by ERA5 reanalysis.

During the wintertime, it becomes more difficult to discriminate between aerosol layers and PSC as previously stated. With maximum SR values above 1.4 around 13–16 km in panels of Figure 7, PSC layers dominated by NAT particles could be assumed, with a range of optical properties overlapping with those of the smoke aerosol (Achtert & Tesche, 2014). Nevertheless, the depolarization ratio below 5% supports the aerosol characterization, as the aged aerosols are expected to reduce their depolarization values (Dahlkötter et al., 2014) whereas equilibrated NAT crystals would have larger depolarization ratios. However, Supercooled Ternary Solution (STS) PSCs can present such SR values with depolarization values close to 0 (Achtert & Tesche, 2014). On the left panels of Figures 7c and 7d, T_{NAT} is shown in purple dashed line. On Figure 7c, temperatures from both radiosonde and ERA5 are above T_{NAT}, except for the layer around 17 km, where the temperature is close to T_{NAT}. However at this altitude, the depolarization ratio is close to 0 which would tend to advocate for a STS PSC but such PSCs are expected to occur several degrees below T_{NAT}. Therefore, we consider these layers as aerosols.

In Figure 7d, temperatures from both radiosonde and ERA5 are below T_{NAT}. Unfortunately, the radiosonde bursted as early as 16,5 km. Between the tropopause and 18 km, depolarization ratio peaks at 2.7% at 14.3 km and at 4% at 17 km, which could correspond to NAT or STS PSCs given the uncertainty of $\delta(z)$ and the strongly depolarizing cirrus layer at 10 km. On the other hand, temperatures from the radiosonde present a local peak at 11.25 km and 13.5 km which is not to be expected in presence of a PSC. These local temperature peaks, even

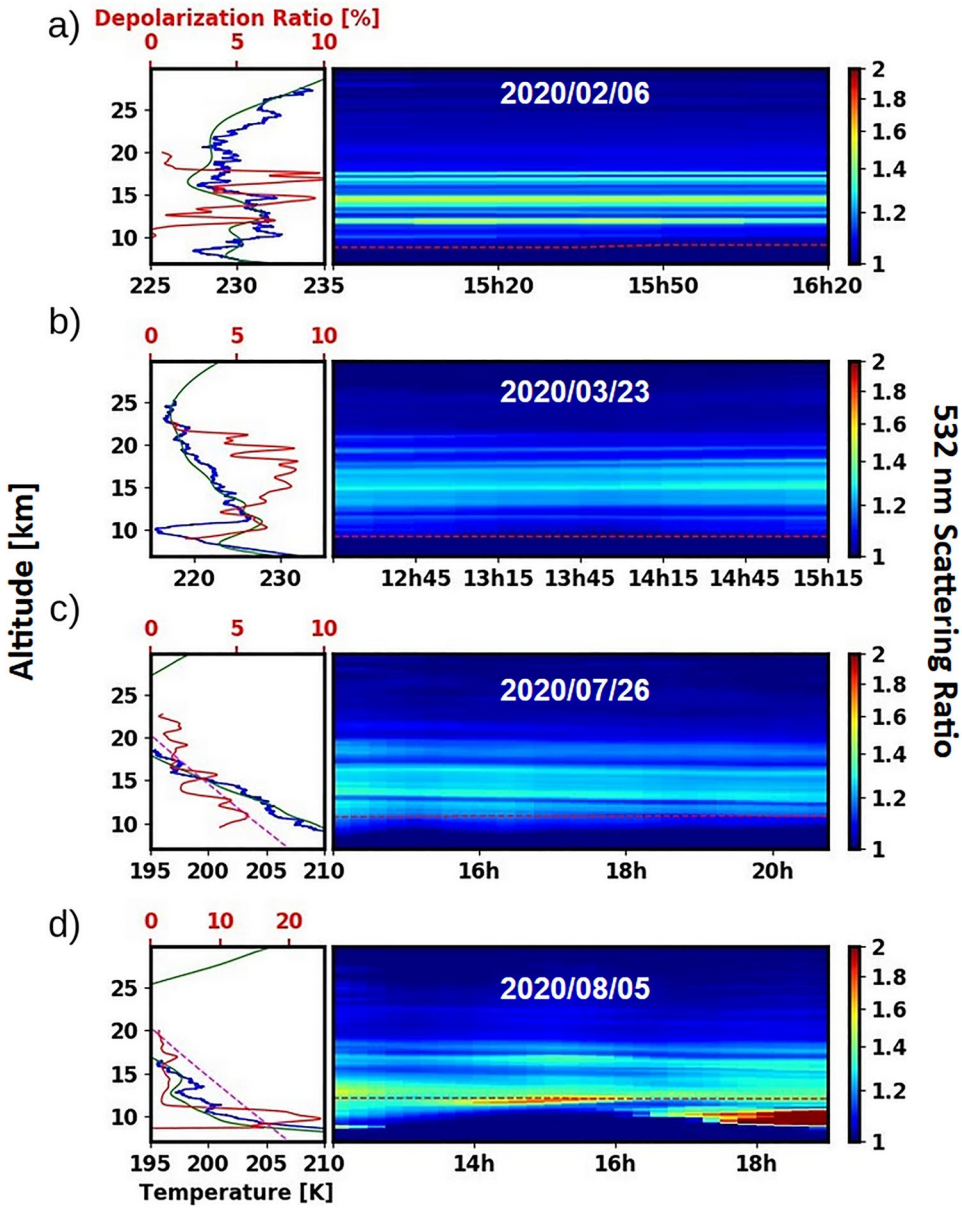

Figure 7. Lidar curtains 532 nm backscatter ratio derived from measurements conducted at Dumont D'Urville (DDU) on 2020/06/02 (a), 2020/03/23 (b), 2020/07/26 (c) and 2020/08/05 (d). The dashed red line indicates the location of the tropopause. On the left, depolarization ratio profiles averaged on the daily sessions are presented (red lines). Temperature profiles from radiosondes launched at DDU as well as from ERA5 reanalysis are shown in blue and green lines respectively. T_{NAT} temperature threshold is shown in purple dashed line.

though below T_{NAT}, illustrate again the difficulty of sorting out PSC and aerosol layers and prevent us from drawing clear conclusions.

The separation between aerosol and PSC would require advanced analysis and accurate speciation between carbon and sulfur out of reach of the data presented in the current paper, especially considering the possible interaction between carbonaceous aerosols and different PSC types do not seem to have been investigated up to now. The scientific question about any impact on PSC microphysics from aerosol presence in the medium still appears relevant and we consider it to be one of the highlights of this paper.

In 2020, the first PSC is reported on 06/23, starting point of the PSC season. The length of the PSC season, which is correlated to temperature and PSC field persistence, is a strong indicator of stratospheric ozone depletion.

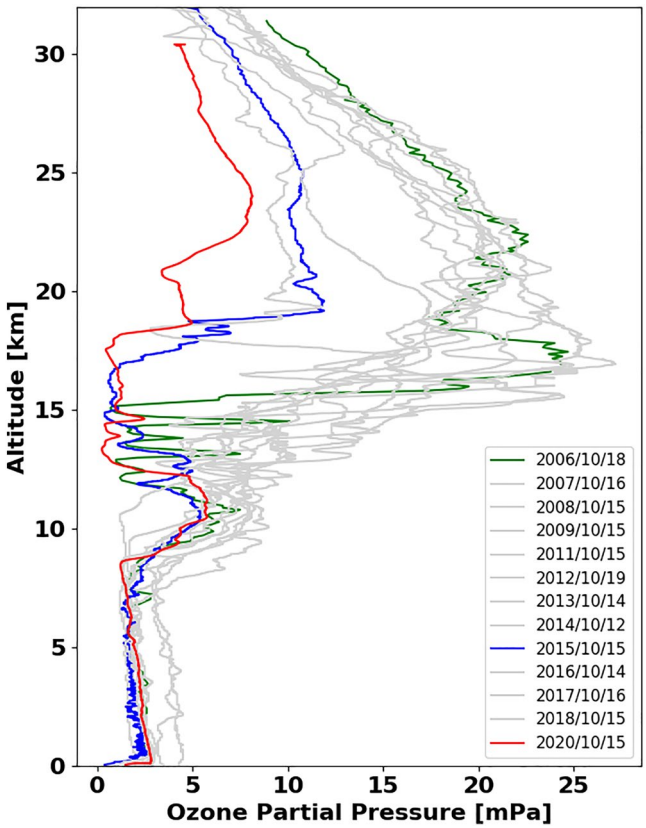

Figure 8. Ozone partial pressure (mPa) measurements from ozone sondes launched at Dumont dUrville in mid-October from 2006 to 2020. Profiles corresponding to 2006, 2015, and 2020 are highlighted, respectively, in green, blue, and red.

PSC fields are observed throughout the wintertime with a final observation in early September. Despite a strong yearly variability, this duration of more than 2 months of PSC presence is in the average of the past decade at DDU. However, ozone measurements from ozone sondes launched at DDU in mid-October from 2006 to 2020 show a significant ozone depletion in 2020 only comparable to the one of 2015. Ozone concentration profiles are shown in Figure 8. In 2015, important aerosol layers coming from the Calbuco eruption were also detected at DDU (data on the NDACC online repository). For the record, the reference 2006 critical ozone depletion profile is also featured in Figure 8. The pattern and vertical range of the depletion still separate it from those observed in 2015 and 2020. This anomalous ozone depletion in mid-October at DDU is in agreement with the findings of Yu et al. (2021) who modeled the impact of the stratospheric smoke injection of the Black Summer event on ozone. Finally, stratospheric ozone depletion is kinetically fast regarding PSC persistence so any aerosol impact would more likely be indirectly related to easier PSC nucleation, but again, these are just preliminary statements (Tritscher et al., 2021).

While the PSC season complicates the tracking of the aerosol plumes, during the Fall season we acquired a significant amount of data to conclude on the optical properties of the smoke aerosols that were transported above the DDU station. From the lidar SR profiles, the aerosol layers appear isolated in Figure 9. Figure 9a shows the SR values of these layers as a function of the day of year (doy) in 2020 and of the depolarization ratio. The doy is used because studying the Black Summer 2019–2020, it reflects the number of days after the main pyroCb events on New Year's eve (Khaykin et al., 2020). In Figure 9b, the SR values of the aerosol layers are plotted against their respective altitude, the months are color-coded.

In Figures 9a and 9b, the time evolution of the optical properties can be followed, as the SR values of the aerosols decrease (from around 1.9 to 1.2) as well as the depolarization ratio values (from 12% to 6%). Our first measurements of these aerosols, ~19 days after the injection, had a SR of 1.9 and a depolarization ratio of 12%. In early June, before the beginning of winter, the aerosol layers showed an average SR of approximately 1.2 and a depolarization ratio around 6.8%. Figure 9b shows the time evolution of the aerosol layer altitudes. The first aerosol layer is detected at 13.5 km. After that, the aerosol layers spread in altitude in February and March and finally converged between 12 and 15 km during May and June.

It is worth noting that the 532 nm SR values observed throughout the considered period are actually low and comparable to small and moderate volcanic plume values especially after weeks of transport (below around 1.5 – Bègue et al., 2017; Khaykin et al., 2018). Still, the Antarctic stratosphere is actually outside any volcanic influence at this time and the DDU position is too far from anthropogenic pollution sources. In the light of the increasing frequency of PyroCb events, it is of interest to compare our results for this particular event with the literature. Table 1 gathers the optical properties of stratospheric smoke plumes reported in recent years. Four different events are listed: the 1998 wildfires in the Northwest Territories, Canada (Fromm et al., 2005), Black Saturday 2009 in Australia (Jumelet et al., 2020), British Columbia wildfires of 2017 (Baars et al., 2019; Hu et al., 2019; Khaykin et al., 2018) and finally the focus of our present study, Black Summer 2020 (Ohneiser et al., 2020).

From Table 1, the variability of SR and backscatter coefficient (β_{aer}) values is high, which could be somewhat expected as there are several impactful variables: the amount of material uplifted during the event, duration of transport and distance between injection and measurement points, and lidar time integration as well as different signal processing chains. Overall, Table 1 still confirms that our values acquired at high latitudes are smaller than values at mid-latitudes, even if within the range of other measurements. The very high SR value reported in Khaykin et al. (2018) is also stated to be uncommon. Conversion from backscatter coefficient to scattering

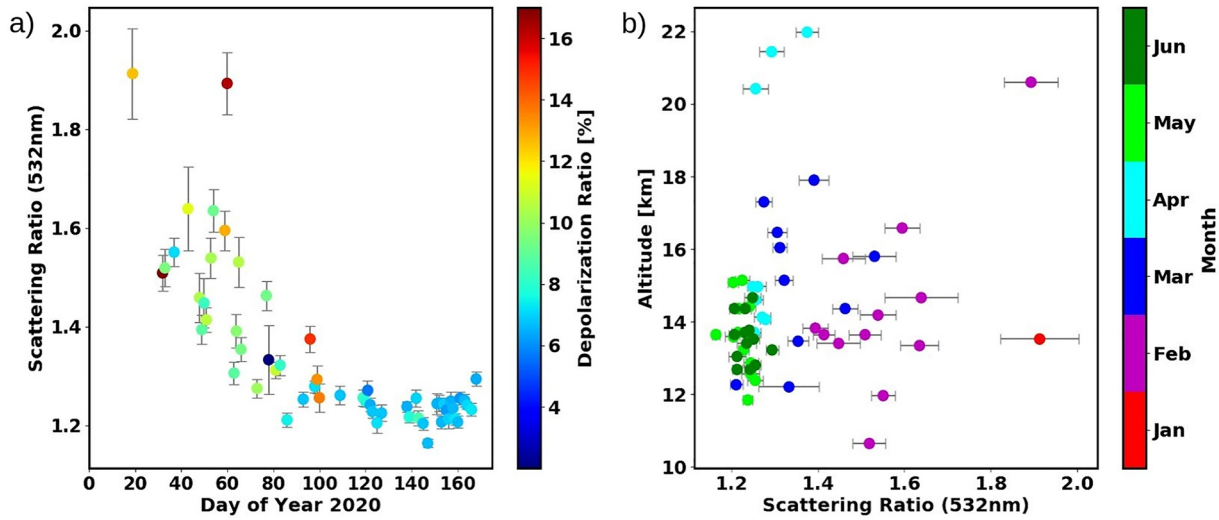

Figure 9. (a) Scatter plot of the identified aerosol layers from January–June 2020 plotted as the scattering ratio versus the day of year (doy) in 2020. The color represents the particulate depolarization ratio, in percentage. (b) Scatter plot of the scattering ratio of each aerosol layer in 2020 plotted as a function of altitude. The color represents the months of 2020. SR uncertainties are calculated from backscatter coefficient errors as a function of lidar data time integration and background sky conditions, considering other error uncertainties constant.

coefficient is not made in Table 1 because of the strong impact of the molecular scattering and the requirement of exact temperature and pressure profiles in each case. Overall, the comparison of our measurements with the literature highlights the duration of the aerosol observations in our study. To our knowledge, it is the first time that a smoke-originated aerosol load is sounded for such a long time period from a single ground-based instrument at high latitudes. There are two main reasons for that: first the pyroCb injections are very impactful (Kablick et al., 2020; Khaykin et al., 2020) and therefore the aerosol load is large enough to be consistently transported toward Antarctica (Figures 2 and 4), and second, once at high latitudes, the round air mass circulation around the pole traps the particles (see Annex 1 for example), which is not the case at lower latitudes, allowing us to sound the aerosol layers for a long period of time.

Table 1
Optical Properties of Stratospheric Smoke Particles From the Literature

	Event	Age (days)	$\beta_{aer} \times 10^{-3}$ km^{-1}sr^{-1}	SR	δ_{aer} (%)	LR (*sr*)	Site
Fromm et al. (2005)	Canada 1998	19	—	1.85	—	—	Sondrestromfjord, Greenland
Hu et al. (2019)	BC 2017	12	4	—	20	54	Lille, France
Hu et al. (2019)	BC 2017	16	2.2	—	—	58	Palaiseau, France
Khaykin et al. (2018)	BC 2017	17	—	8	—	—	OHP, France
Baars et al. (2019)	BC 2017	28	0.075	—	16	65	Limassol, Cyprus
Jumelet et al. (2020)	Austr. 2009	22	—	1.4	—	—	DDU, Adélie Land
Jumelet et al. (2020)	Austr. 2009	24	—	1.55	—	—	DDU, Adélie Land
Ohneiser et al. (2020)	Austr. 2020	9	1.4	—	15	76	Punta Arenas, Chile
Tencé 2021	Austr. 2020	19	0.25	1.91	12.6	87	DDU, Adélie Land
Tencé 2021	Austr. 2020	32	0.135	1.51	17	73	DDU, Adélie Land
Tencé 2021	Austr. 2020	120	0.057	1.25	7	—	DDU, Adélie Land

Note. BC 2017 refers to British Columbia wildfires of 2017, Austr. 2009 refers to 2009 Black Saturday. Age is time elapsed from the event. β_{aer} is the aerosol backscatter coefficient, in km^{-1}sr^{-1}. δ_{aer} is the aerosol depolarization ratio and LR is the lidar ratio.

5. Conclusion

The Australian 2019–2020 fire season is exceptional both in duration and extent with numerous pyroCb events reported to inject an unprecedented amount of combustion aerosols into the southern hemispheric stratosphere. In this paper, we characterize the patches of smoke that reached the Antarctic region using a combination of satellite measurements from OMI, OMPS, and MLS and a unique ground-based lidar measurement record covering the entire lifetime of Australian wildfire smoke in the Antarctic stratosphere. Starting mid-January, throughout the PSC season and up to the latest measurements in October, the lidar located at the French Antarctic station DDU monitored a persistent stratospheric aerosol layer with optical properties clearly distinct from that of the background sulphate aerosol signatures. The combination of spaceborne mesoscale UV aerosol index (OMI), visible extinction (OMPS), and backward trajectory modeling confirm these particles originate from the Australian PyroCb events.

The reported measurements are a valuable contribution to the characterization of the optical properties of aged smoke particles while being, as far as we are aware of, the longest observed smoke aerosol time series recorded at stratospheric altitudes. We point out the persistence of smoke aerosols in the southern high latitude stratosphere following the mid-latitude wildfire events, which is already acknowledged for volcanic eruptions. Further investigations are needed to finely resolve speciation between sulfated and carbonaceous aerosols or between aerosols layers.

Therefore, it is out of the scope of this paper to investigate deeper into microphysical interactions between different aerosol types and PSC nucleation. For the record and to support further studies, the 2020 stratospheric ozone depletion season is above the decade's average at DDU, and comparable to 2015, a year featuring a volcanic aerosol detection recorded at DDU.

While satellite measurements are mandatory to complement statements on the aerosol nature and origin, the associated uncertainties are still high enough so that we think only ground-based detection can provide more quantitative insight into the properties of the particles, especially at high latitudes where data availability from various spaceborne instruments have been poorly evaluated and where in-situ campaigns featuring particle counters or balloon-borne sondes remain rare. Keeping up with ground-based facilities and monitoring stations at high latitudes remains highly valuable as the optical properties of thin filamentary smoke layers are often close to the satellite sensor sensitivity which can make them barely visible or harder to investigate. A complementary array of spectral channels to derive microphysical parameters at very high time and vertical resolution of the lidar instrument remain for us the key asset in the study of stratospheric aerosols.

Besides, and in the overall frame of a warmer climate, the prerequisites to major wildfire events such as the Australian Black Summer will be more frequently reached (Hennessy, 2006; Lucas et al., 2007) and this further strengthens the scientific interest in investigations on the global scale impact of smoke aerosols, especially at high latitudes where the stratospheric aerosols will mostly remain confined above Antarctica. The subsequent sedimentation process of the particles could also lead to some degree of snow or ice sheets albedo alteration. Considering larger time scales, such processes may have had past climatic impacts and be a factor to help explain a faster than predicted evolution of ice sheets melting. The present paper highlights the processes involving fine aerosol plumes and transport to high latitudes that are not properly modeled in climate models, being either on the subgrid scale or not even parametrized. An adequate inclusion of these processes could lead to significant local atmospheric or even surface impacts considering the larger scale of the related events.

Data Availability Statement

The lidar instrument is part of the NDACC international network and data are publicly available online at the NDACC/NOAA data archive (ftp://ftp.cpc.ncep.noaa.gov/ndacc/station/dumont/ames/), as well as on the AERIS database (http://cds-espri.ipsl.fr/).

Acknowledgments
Operations on the Dumont d'Urville station are supported by the French polar institute (Institut polaire français Paul-Emile Victor), science project 209. The authors gratefully acknowledge the NOAA Air Resources Laboratory (ARL) for the provision of the HYSPLIT transport and dispersion model and/or READY website (https://www.ready.noaa.gov) used in this publication.

References

Achtert, P., & Tesche, M. (2014). Assessing lidar-based classification schemes for polar stratospheric clouds based on 16 years of measurements at esrange, Sweden. *Journal of Geophysical Research: Atmospheres*, *119*(3), 1386–1405. https://doi.org/10.1002/2013JD020355

Adams, M. A., Shadmanroodposhti, M., & Neumann, M. (2020). Causes and consequences of eastern Australia's 2019–20 season of mega-fires: A broader perspective. *Global Change Biology*, *26*(7), 3756–3758. https://doi.org/10.1111/gcb.15125

Ansmann, A., Wandinger, U., Riebesell, M., Weitkamp, C., & Michaelis, W. (1992). Independent measurement of extinction and backscatter profiles in cirrus clouds by using a combined Raman elastic-backscatter lidar. *Appl. Opt.*, *31*, 7113–7131. https://doi.org/10.1364/AO.31.007113

Baars, H., Ansmann, A., Ohneiser, K., Haarig, M., Engelmann, R., Althausen, D., & Pappalardo, G. (2019). The unprecedented 2017–2018 stratospheric smoke event: Decay phase and aerosol properties observed with the earlinet. *Atmospheric Chemistry and Physics*, *19*(23), 15183–15198. https://doi.org/10.5194/acp-19-15183-2019

Bègue, N., Vignelles, D., Berthet, G., Portafaix, T., Payen, G., Jégou, F., et al. (2017). Long-range transport of stratospheric aerosols in the southern hemisphere following the 2015 calbuco eruption. *Atmospheric Chemistry and Physics*, *17*(24), 15019–15036. https://doi.org/10.5194/acp-17-15019-2017

Behrendt, A., & Nakamura, T. (2002). Calculation of the calibration constant of polarization lidar and its dependency on atmospheric temperature. *Opt. Express*, *10*. https://doi.org/10.1364/OE.10.000805

Borchers Arriagada, N., Palmer, A., Bowman, D. M., Morgan, G., Jalaludin, B., & Johnston, F. (2020). Unprecedented smoke-related health burden associated with the 2019–20 bushfires in eastern Australia. *Medical Journal of Australia*, *17*(24), 15019–15036. https://doi.org/10.5694/mja2.50545

Cai, W., Cowan, T., & Raupach, M. (2009). Positive Indian Ocean dipole events precondition southeast Australia bushfires. *Geophysical Research Letters*, *36*, L19710. https://doi.org/10.1029/2009GL039902

Charlson, R., Schwartz, S., Hales, J., Cess, R., Coakley, J., Hansen, J., & Hofmann, D. (1992). Climate forcing by anthropogenic aerosols. *Science (New York, N.Y.)*, *255*, 423–430. https://doi.org/10.1126/science.255.5043.423

Chazette, P., David, C., Lefrère, J., Godin, S., Pelon, J., & Mégie, G. (1995). Comparative lidar study of the optical, geometrical, and dynamical properties of stratospheric post-volcanic aerosols, following the eruptions of El Chichon and Mount Pinatubo. *Journal of Geophysical Research: Atmospheres*, *100*. https://doi.org/10.1029/95JD02268

Chen, Z., Bhartia, P. K., Loughman, R., Colarco, P., & DeLand, M. (2018). Improvement of stratospheric aerosol extinction retrieval from omps/lp using a new aerosol model. *Atmospheric Measurement Techniques*, *11*(12), 6495–6509. https://doi.org/10.5194/amt-11-6495-2018

Cheney, N. (1976). Bushfire disasters in Australia, 1945–1975. *Australian Forestry*, *39*(4), 245–268. https://doi.org/10.1080/00049158.1976.10675654

Clarke, H., Lucas, C., & Smith, P. (2013). Changes in australian fire weather between 1973 and 2010. *International Journal of Climatology*, *33*(4), 931–944. https://doi.org/10.1002/joc.3480

Dahlkötter, F., Gysel, M., Sauer, D., Minikin, A., Baumann, R., Seifert, P., et al. (2014). The pagami creek smoke plume after long-range transport to the upper troposphere over europe - Aerosol properties and black carbon mixing state. *Atmospheric Chemistry and Physics*, *14*(12), 6111–6137. https://doi.org/10.5194/acp-14-6111-2014

Davey, S., & Sarre, A. (2020). Editorial: The 2019/20 Black Summer bushfires. *Australian Forestry*, *83*(2), 47–51. https://doi.org/10.1080/00049158.2020.1769899

David-Beausire, C., Bekki, S., Godin-Beekmann, S., Mégie, G., & Chipperfield, M. (1998). Polar stratospheric clouds climatology over Dumont d'urville between 1989 and 1993 and the influence of volcanic aerosols on their formation. *Journal of Geophysical Research*, *1032*, 22163–22180. https://doi.org/10.1029/98JD01692

David, C., Haefele, A., Keckhut, P., Marchand, M., Jumelet, J., Leblanc, T., et al. (2012). Evaluation of stratospheric ozone, temperature, and aerosol profiles from the LOANA lidar in Antarctica. *Polar Science*, *6*, 209–225. https://doi.org/10.1016/j.polar.2012.07.001

Dowdy, A., Fromm, M., & McCarthy, N. (2017). Pyrocumulonimbus lightning and fire ignition on black saturday in southeast Australia. *Journal of Geophysical Research: Atmospheres*, *122*(14), 7342–7354. https://doi.org/10.1002/2017JD026577

Dowdy, A., Ye, H., Pepler, A., Thatcher, M., Osbrough, S., Evans, J., et al. (2019). Future changes in extreme weather and pyroconvection risk factors for australian wildfires. *Scientific Reports*, *9*, 10073. https://doi.org/10.1038/s41598-019-46362-x

Fernald, F. G. (1984). Analysis of atmospheric lidar observations: Some comments. *Applied Optics*, *23*(5), 652–653. https://doi.org/10.1364/AO.23.000652

Fiebig, M., Lunder, C. R., & Stohl, A. (2009). Tracing biomass burning aerosol from south America to troll research station, Antarctica. *Geophysical Research Letters*, *36*(14), L14815. https://doi.org/10.1029/2009GL038531

Flynn, L., Long, C., Wu, X., Evans, R., Beck, C. T., Petropavlovskikh, I., & Seftor, C. (2014). Performance of the ozone mapping and profiler suite (omps) products. *Journal of Geophysical Research: Atmospheres*, *119*(10), 6181–6195. https://doi.org/10.1002/2013JD020467

Fromm, M., Bevilacqua, R., Servranckx, R., Rosen, J., Thayer, J. P., Herman, J., & Larko, D. (2005). Pyro-cumulonimbus injection of smoke to the stratosphere: Observations and impact of a super blowup in northwestern Canada on 3–4 August 1998. *Journal of Geophysical Research: Atmospheres*, *110*(D8), D08205. https://doi.org/10.1029/2004JD005350

Fromm, M., Lindsey, D., Servranckx, R., Yue, G., Trickl, T., Sica, R., et al. (2010). The untold story of pyrocumulonimbus. *Bulletin of the American Meteorological Society*, *91*(9), 1193–1210. https://doi.org/10.1175/2010BAMS3004.1

Fromm, M., Tupper, A., Rosenfeld, D., Servranckx, R., & McRae, R. (2006). Violent pyro-convective storm devastates Australia's capital and pollutes the stratosphere. *Geophysical Research Letters*, *33*, L05815. https://doi.org/10.1029/2005GL025161

Hennessy, K. (2006). Climate change impacts on fire-weather in south-east Australia. In *The joint AFAC/IFCAA bushfire CRC conference: 10-13 August 2006: Melbourne convention centre Australia: Conference proceedings* (pp. 536–546). Bushfire CRC.

Hirsch, E., & Koren, I. (2021). Record-breaking aerosol levels explained by smoke injection into the stratosphere. *Science*, *371*, 1269-1274. https://doi.org/10.1126/science.abe1415

Hu, Q., Goloub, P., Veselovskii, I., Bravo-Aranda, J.-A., Popovici, I. E., Podvin, T., & Chen, C. (2019). Long-range-transported Canadian smoke plumes in the lower stratosphere over northern France. *Atmospheric Chemistry and Physics*, *19*(2), 1173–1193. https://doi.org/10.5194/acp-19-1173-2019

Jaross, G., Bhartia, P. K., Chen, G., Kowitt, M., Haken, M., Chen, Z., & Kelly, T. (2014). Omps limb profiler instrument performance assessment. *Journal of Geophysical Research: Atmospheres*, *119*(7), 4399–4412. https://doi.org/10.1002/2013JD020482

Jumelet, J., Klekociuk, A. R., Alexander, S. P., Bekki, S., Hauchecorne, A., Vernier, J. P., & Keckhut, P. (2020). Detection of aerosols in Antarctica from long-range transport of the 2009 australian wildfires. *Journal of Geophysical Research: Atmospheres*, *125*(23), e2020JD032542. https://doi.org/10.1029/2020JD032542

Kablick, G., III, Allen, D., Fromm, M., & Nedoluha, G. (2020). Australian pyrocb smoke generates synoptic-scale stratospheric anticyclones. *Geophysical Research Letters*, *47*(13), e2020GL088101. https://doi.org/10.1029/2020GL088101

Khaykin, S., Godin-Beekmann, S., Hauchecorne, A., Pelon, J., Ravetta, F., & Keckhut, P. (2018). Stratospheric smoke with unprecedentedly high backscatter observed by lidars above southern France. *Geophysical Research Letters*, *45*(3), 1639–1646. https://doi.org/10.1002/2017GL076763

Khaykin, S., Legras, B., Bucci, S., Sellitto, P., Isaksen, L., Tencé, F., et al. (2020). The 2019/20 Australian wildfires generated a persistent smoke-charged vortex rising up to 35km altitude. *Communications Earth & Environment*, *1*(1), 22. https://doi.org/10.1038/s43247-020-00022-5

Klett, J. D. (1981). Stable analytical inversion solution for processing lidar returns. *Applied Optics*, *20*(2), 211–220. https://doi.org/10.1364/AO.20.000211

Klett, J. D. (1985). Lidar inversion with variable backscatter/extinction ratios. *Applied Optics*, *24*(11), 1638–1643. https://doi.org/10.1364/AO.24.001638

Kloss, C., Berthet, G., Sellitto, P., Ploeger, F., Taha, G., Tidiga, M., et al. (2021). Stratospheric aerosol layer perturbation caused by the 2019 Raikoke and Ulawun eruptions and their radiative forcing. *Atmospheric Chemistry and Physics*, *21*, 535–560. https://doi.org/10.5194/acp-21-535-2021

Kremser, S., Thomason, L. W., von Hobe, M., Hermann, M., Deshler, T., Timmreck, C., & Meland, B. (2016). Stratospheric aerosol: Observations, processes, and impact on climate. *Reviews of Geophysics*, *54*(2), 278–335. https://doi.org/10.1002/2015RG000511

Levelt, P., Oord, G., Dobber, M., Mälkki, A., Visser, H., Vries, J., et al. (2006). The ozone monitoring instrument. *IEEE T. Geoscience and Remote Sensing*, *44*, 1093–1101. https://doi.org/10.1109/TGRS.2006.872333

Lim, E., Hendon, H., Boschat, G., Hudson, D., Thompson, D. W., Dowdy, A., & Arblaster, J. (2019). Australian hot and dry extremes induced by weakenings of the stratospheric polar vortex. *Nature Geoscience*, *12*, 896–901. https://doi.org/10.1038/s41561-019-0456-x

Livesey, N. J., Read, W. G., Lambert, A., Cofield, R. E., Cuddy, D. T., Froidevaux, L., et al. (2007). *Eos mls version 2.2 level 2 data quality and description document, technical report*. Jet Propulsion Laboratory D-33509.

Lucas, C., Hennessy, K. J., Mills, G. A., & Bathols, J. M. (2007). *Bushfire weather in southeast Australia recent trends and projected climate change impacts ; consultancy report prepared for the climate institute of Australia. Bushfire Cooperative Research Centre*. Australian Bureau of Meteorology and CSIRO Marine and Atmospheric Research. https://doi.org/10.25919/5e31c82ee0a4c

Martinsson, B., Friberg, J., Sandvik, O., Hermann, M., van Velthoven, P., & Zahn, A. (2019). Formation and composition of the UTLS aerosol. *NPJ Climate and Atmospheric Science*, *2*, 40. https://doi.org/10.1038/s41612-019-0097-1

McArthur, A. (1967). *Causes and consequences of eastern Australia's 2019–20 season of mega-fires: A broader perspective*. Forest Research Institute, Forestry and Timber Bureau, Leaflet No. 107.

McRae, R., Sharples, J., & Fromm, M. (2015). Linking local wildfire dynamics to pyrocb development. *Natural Hazards and Earth System Sciences*, *15*(3), 417–428. https://doi.org/10.5194/nhess-15-417-2015

Nolan, R., Boer, M., Collins, L., Resco de Dios, V., Clarke, H., Jenkins, M., et al. (2020). Causes and consequences of eastern Australia's 2019-20 season of mega-fires. *Global Change Biology*, *26*(3), 1039–1041. https://doi.org/10.1111/gcb.14987

Ohneiser, K., Ansmann, A., Baars, H., Seifert, P., Barja, B., Jimenez, C., et al. (2020). Smoke of extreme Australian bushfires observed in the stratosphere over Punta Arenas, Chile, in January 2020: Optical thickness, lidar ratios, and depolarization ratios at 355 and 532 nm. *Atmospheric Chemistry and Physics Discussions*, *20*(13), 8003–8015. https://doi.org/10.5194/acp-2020-96

Penner, J., Andreae, M., & Annegarn, M. (2001). Aerosol, their direct and indirect effets, In: *Climate change 2001: The scientific basis. Contribution of Working Group I to the Third Assessment report of the Intergovernmental panel on climate change*, 5, 291–336.

Peterson, D., Fromm, M., McRae, R. H. D., Campbelle, J. R., Hyer, E. J., Taha, G., et al. (2021). Australia's black summer pyrocumulonimbus super outbreak reveals potential for increasingly extreme stratospheric smoke events. *NPJ Climate and Atmospheric Science*, *4*(38), 2235–2255. https://doi.org/10.1038/s41612-021-00192-9

Peterson, D., Hyer, E., Campbell, J., Solbrig, J., & Fromm, M. (2017). A conceptual model for development of intense pyrocumulonimbus in western North America. *Monthly Weather Review*, *145*(6), 2235–2255. https://doi.org/10.1175/MWR-D-16-0232.1

Rault, D., & Loughman, R. P. (2013). The omps limb profiler environmental data record algorithm theoretical basis document and expected performance. *Geoscience and Remote Sensing, IEEE Transactions on*, *51*, 2505–2527. https://doi.org/10.1109/TGRS.2012.2213093

Rolph, G., Stein, A., & Stunder, B. (2017). Real-time environmental applications and display system: Ready. *Environmental Modelling & Software*, *95*, 210–228. https://doi.org/10.1016/j.envsoft.2017.06.025

Safieddine, S., Bouillon, M., Paracho, A., Jumelet, J., Tencé, F., Pazmino, A., et al. (2020). Antarctic ozone enhancement during the 2019 sudden stratospheric warming event. *Geophysical Research Letters*, *47*(14), e2020GL087810. https://doi.org/10.1029/2020GL087810

Sharples, J., Cary, G., Fox-Hughes, P., Mooney, S., Evans, J., Fletcher, M., et al. (2016). Natural hazards in Australia: Extreme bushfire. *Climatic Change*, *139*, 85–99. https://doi.org/10.1007/s10584-016-1811-1

Stein, A., Draxler, R., Rolph, G., Stunder, B., Cohen, M., & Ngan, F. (2016). NOAA's hysplit atmospheric transport and dispersion modeling system. *Bulletin of the American Meteorological Society*, *96*(12), 2059–2077. https://doi.org/10.1175/BAMS-D-14-00110.1

Torres, O., Tanskanen, A., Veihelmann, B., Ahn, C., Braak, R., Bhartia, P. K., & Levelt, P. (2007). Aerosols and surface UV products from ozone monitoring instrument observations: An overview. *Journal of Geophysical Research*, *112*(D24), D24S47. https://doi.org/10.1029/2007JD008809

Tory, K., Thurston, W., & Kepert, J. (2018). Thermodynamics of pyrocumulus: A conceptual study. *Monthly Weather Review*, *146*(8), 2579–2598. https://doi.org/10.1175/MWR-D-17-0377.1

Tritscher, I., Pitts, M. C., Poole, L. R., Alexander, S. P., Cairo, F., Chipperfield, M. P., et al. (2021). Polar stratospheric clouds satellite observations, processes, and role in ozone depletion. *Reviews of Geophysics*, *59*(2), e2020RG000702. https://doi.org/10.1029/2020RG000702

Waters, J. W., Froidevaux, L., Harwood, R. S., Jarnot, R. F., Pickett, H. M., Read, W. G., & Walch, M. J. (2006). The earth observing system microwave limb sounder (EOS MLS) on the aura satellite. *IEEE Transactions on Geoscience and Remote Sensing*, *44*(5), 1075–1092. https://doi.org/10.1109/TGRS.2006.873771

Yu, P., Davis, S. M., Toon, O. B., Portmann, R. W., Bardeen, C. G., Barnes, J. E., & Rosenlof, K. H. (2021). Persistent stratospheric warming due to 2019–2020 Australian wildfire smoke. *Geophysical Research Letters*, *48*(7), e2021GL092609. https://doi.org/10.1029/2021GL092609